communications materials

Article

https://doi.org/10.1038/s43246-024-00706-x

Fabrication of bendable and narrow bandgap $Cu(In,Ga)(S,Se)_2$ for tandem photovoltaics

Sarallah Hamtaei[1,2,3], Alice Debot[4], Romain Scaffidi[1,2,3,5], Guy Brammertz[1,2,3], Estelle Cariou[1,3], Sean M. Garner[6], Aranzazu Aguirre[1,2,3], Jef Poortmans[1,2,3,7], Phillip J. Dale[4] & Bart Vermang[1,2,3]

$Cu(In,Ga)(S,Se)_2$ absorbers with a bandgap in the near-infrared region are ideal candidates for a bottom cell in multi-junction solar cell architectures. In flexible and lightweight form factors, such devices could help power many applications through integrated solar cells. Here, we show the use of a two-step method to synthesize $Cu(In,Ga)(S,Se)_2$, with a bandgap between 1.00 and 1.13 eV, on bendable ultra-thin glass, with minority carrier lifetimes approaching 100 ns, in a homogenous and repeatable fashion. We also report on conventional and alternative device fabrication methods with very low waste and toxicity footprints. Champion solar cells are fabricated based on absorbers with a graded bandgap between 1.05 and 1.1 eV, and an open circuit voltage approaching 600 mV. Our results show a way for scalable fabrication of all thin-film, flexible tandem solar cells, by means of industrially relevant processing steps in a low cost and sustainable fashion.

What is missing to enable flexible high performing solar cells? Why is that of interest anyway, and where can we find a (part of the) solution?

The fascination with flexible form factors concerns realizing integrated photovoltaic (PV) applications in (self-powered) wearable optoelectronics, biomedical products, internet of things (IoT), and not least, buildings, vehicles, sailboats, and many other applications in need of electrical energy[1]. Nonetheless, moving from rigid concepts to flexibles is challenging. This is in part due to the materials used, their processing paths, and/or device architecture which undermine flexibility in one way or another. E.g., Si photovoltaic technology is very mature and can be found in applications with conventional flat surfaces such as rooftops. However, the brittleness, and particularly heavy modules, make its adaptation to more complex and non-planar surfaces- such as those found in curvy architectures, e.g., a car hatchback, or even consumer products, cumbersome, and at minimum, imposes aesthetic compromises. Part of the solution is in technologies with relatively high specific power (power per unit weight), and in realizing them in flexible form factors. Thin-film tandem solar cells can address such needs; they offer sustained performance under bending stress, high specific power, and competitive economic and ecologic figures of merit[2–4], and thus can help source part of the power needed in applications such as vehicle or buildings, in integrated formats (see e.g., an illustration for BIPV in Fig. 1).

But single junction $Cu(In,Ga)(S,Se)_2$ (CIGS) and organic-inorganic halide perovskites (perovskite) based technologies have had a hard time claiming a double digit market share in the past years, largely due to a combination of comparably lower power conversion efficiency (PCE) at large scale, toxicity issues, or long-term stability, compared to crystalline Si technology[5,6]. Comparatively low PCEs are also the one reason behind their failing to capitalize in the extraterrestrial market. In fact, both CIGS and perovskite thin film technologies have shown decent tolerances to space debris and high radiation conditions in low-temperature/low-intensity environments[7,8]. But neither these, nor an overall cost advantage could make up for their subpar performance relative to III-V based products.

To overcome the single junction performance limits, tandem devices can be developed to harvest a larger spectrum of incident light. Particularly, wide bandgap perovskite in tandem with narrow bandgap CIGS is a promising candidate in double junction architectures[9], and simulations reveal their potential to reach beyond 40% PCE for both 4-terminal and 2-terminal structures[10].

Either way, from a manufacturing perspective, for a 2-terminal tandem device, the bottom cell's (CIGS) roll-to-roll and large-scale production plays the bottle neck role, along with the stability issues of perovskites. One challenge is the synthesis of the CIGS absorber, which requires the highest temperature, far beyond the thermal stability of the upper perovskite sub-

---

[1]imec, imo-imomec, Genk, Belgium. [2]Hasselt University (partner in Solliance), imo-imomec, Hasselt, Belgium. [3]EnergyVille, imo-imomec, Genk, Belgium. [4]Department of Physics and Materials Science, University of Luxembourg, Belvaux, Luxembourg. [5]UCLouvain, ICTEAM, Louvain-la-Neuve, Belgium. [6]Corning Research and Development Corporation, One River Front Plaza, Corning, New York, USA. [7]KU Leuven, Department of Electrical Engineering, Heverlee, Belgium. e-mail: sarallah.hamtaei@imec.be

Fig. 1 | Conceptual drawing of flexible, light-weight PV panels potentially augmented on the Walt Disney Hall in LA, California. Original photo by Carol M. Highsmith, available in public domain.

Table 1 | Surface roughness (S_a) of the metal precursor and absorbers

Metric	Precursor		Absorber		
S_a	CGI	+Se	Bare	+CdS	+In_2S_3
Mean (nm)	186	133	184	147	164
CV (%)	5.7	2.8	1.9	1.7	4.4

Coefficient of variation (CV) is the ratio of standard deviation to the mean of the measurement values.

cell. This leaves two fabrication strategies, either more effective transfer technologies should be developed to detach one of the sub-cells from its original growth surface to stack onto the other sub-cell, or the entire tandem should be fabricated from bottom up; to grow CIGS and use it as a *substrate* to grow the perovskite sub-cell on top. The latter appears to be a more realistic, scalable, and industrial approach.

Another issue arises when using flexibles substrates. The high temperatures required for CIGS growth limit the available substrates which can sustain the harsh growth environment. This is even more pronounced for the two-step sequential method, where higher temperatures are needed (under long durations) compared to co-evaporation routes. Therefore, there is a limited degree of freedom where one can keep the method simple, effective (and not reverting to e.g., co-evaporation with a higher capex and more complex processing) and avoid lowering the growth temperature (and lose its positive influence on material quality/crystallinity), while enjoying an affordable choice of substrate.

As elucidated by Kessler and Rudmann, a primary concern in the choice of substrate is how it matches the rest of the stack in a CIGS device[11]. Most notably, due to the high temperatures the stack experiences in the absorber's growth stage, it is vital for different layers to have similar coefficient of thermal expansion (CTE). Furthermore, the roughness of the substrates translates (to some extent) to surface roughness of the CIGS, and higher layers. For tandem applications, it is then necessary to either smoothen the surface of the CIGS sub cell using chemical and/or mechanical etching techniques, or to use a smooth enough substrate to begin with. Moreover, the substrate can aid light management in the stack by reflecting a spectrum of interest. Coupled with (semi)transparent contact materials, such concepts can lead to development of bi-facial solar cells and improved light harvesting. Lastly, the substrate should ideally not interact with the absorber in the wrong way. I.e., while alkali elements from certain glasses act as dopants, iron from stainless steel could reduce the performances significantly, and introduce complexities to the stack development, which has remained challenging, despite considerable success[12–15].

Ultra-thin glass (UTG) complies with such considerations and is used more and more in optoelectronics industry- not least in thin film photovoltaic technology[16–19]. These are light-weight, and offer a useful degree of bendability at thicknesses below 200 µm. In principle, this makes them an ideal candidate for vehicle integrated PV and high-altitude/ space applications. On the other hand, while most literature focuses on co-evaporation routes to make CIGS on UTG substrates, in this work, we have demonstrated the use of sequential growth, where the metallic stack of constituent elements undergo rapid thermal annealing (RTA) and convert to CIGS film. Here, the advantages of metal deposition and annealing are demonstrated through the ease of process control and studying the homogeneity and quality of the absorbers. Additionally, we reveal the annealing parameters to tune the bandgap of CIGS thinfilm. Furthermore, we report on making high performing devices fabricated through both conventional and more eco-friendlier routes. In particular, CdS is commonly used as a buffer layer in CIGSSe solar cells. However, its toxicity has long been established, and its band gap leads to parasitic absorption, also known as the blue defect. To avoid this, In_2S_3 is used as a possible replacement compared to the traditional CdS[20]. Moreover, CdS is most often deposited through a chemical bath (CBD). However, the waste associated with this technique is non-negligible. In_2S_3 on the other hand, as used in this study, can be inkjet-printed, which produces nearly zero waste[21].

To this end, considering the literature of thin film photovoltaics on ultra-thin glass, here for the first time we study an adjusted, scalable CIGS growth technique, as well as promising non-toxic stack designs (In_2S_3 buffer layer) on ultra-thin glass. Narrow bandgap CIGS absorbers are synthesized on flexible glass coupons, using an adjusted selenization technique adopted from what is used by Avancis[22]. They were then coated with buffer layers of two kinds; either conventional CBD of CdS, or near-zero waste inkjet printing of In_2S_3. The absorbers are characterized in different primary metrics of importance to photovoltaic behavior of the material. To demonstrate the promise of the grown absorbers, two solar cells were made using two different window layer/ grid stacks. A description of the methodology of the work can be found at the end, under the Methods section.

Results and Discussion

At first glance, solar cell devices showed no sign of mechanical instability. To the naked eye, all process steps from the back contact deposition to the front contact evaporation were carried out with no indications of delamination or cracks. Selenization annealing of the metallic precursor resulted in a slightly concave curvature, which hints at compressive stress in the substrate, compared to the tensile stress at the (Mo/)CI(G)Se interface due to mismatch in the coefficient of thermal expansion[23,24]. This could also have resulted from annealing temperatures close to annealing point of the substrate (550 °C), which roughly speaking is when the glass starts to relax the residual stress.

Observing the sample with naked eye after each step of the process flow (before device fabrication) suggests a spatially homogenous growth that indicates possibly similar roughness values across different areas. To quantitatively assess this, Sa roughness values were extracted using a confocal microscope (with 10 nm sensitivity) after precursor sputtering, Se evaporation, absorber growth, and post buffer deposition, on four randomly chosen and widely separated locations, with each measurement covering an area of nearly 50 × 50 µm^2—see summarized results in Table 1. Except for the CGI deposition, every processing step resulted in very low roughness, with below 6% coefficient of variation (CV) in different steps, at rather low absolute values considering the growth technique. Besides, much roughness might come from the precursor and has less to do with the RTA process. This can be reasoned by comparing the mean values of metal precursors and bare absorbers, which are only 2 nm apart.

To put these values into perspective, Kafedjiska et al., report on integration of CIGS absorbers with Sq of 120 nm, into a high performing tandem device[25]. Next to thickening of absorbers, other strategies such as smoothening of the eventual TCO layer appear to be more reliable pathways to further reduce the roughness of bottom cells[26].

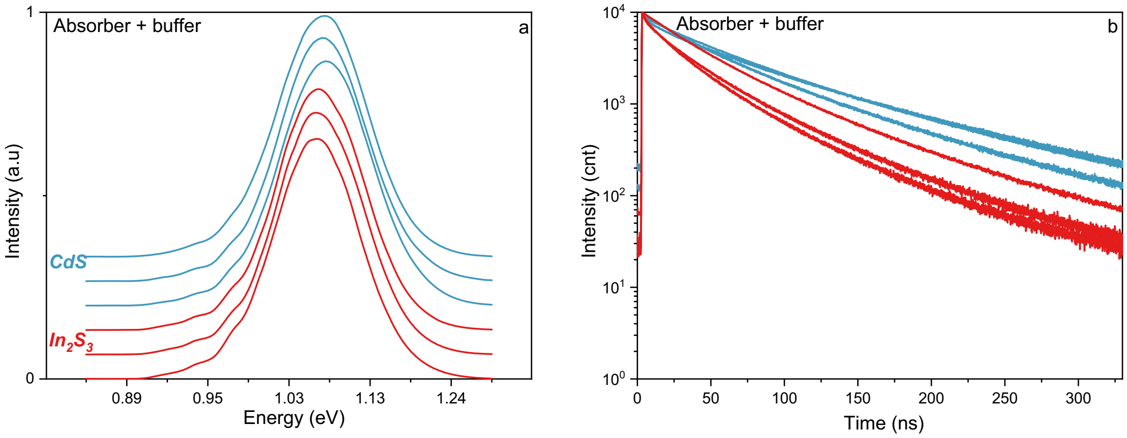

Fig. 2 | Room temperature photoluminescence (PL) response of CIGSSe absorber. a PL spectra of the chosen bandgap, measured after buffer deposition on three different areas, and (**b**) corresponding Time-Resolved PL (TRPL) measurements.

Two micrometers of evaporated Se understandably cover the rough surface of the precursor and fill the valleys, which is the probable cause behind lower measured S_a values. The same reasoning is behind the reduction in roughness when the buffer is deposited. Still, the CBD CdS appears to provide a more continuous film, compared to the inkjet printing of In_2S_3, with overall smoother (mean), and more homogenous morphologies (lower CV).

Another indication of process homogeneity and repeatability is in PL spectroscopy response of buffer covered absorbers, which indicates a growth with minimal peak position variation within a sample, and across different replicas. Moreover, using annealing process tuning, the bandgap of the absorber (as determined by PL measurement) could be tuned between 1.13 and 1.00 eV (Supplementary Fig. 1b). Such a range could be realized through mainly changing heat-up and cool-down ramp rates (between 5 °C/s and 0.5 °C/s) and sulfurization conditions (pressure, between 50 and 100 mbar, and duration, between 1 min and 5 min), which we assume impact the distribution and content of Ga and S, respectively. In particular, either slower heat-up ramps, slower cool-down ramps and/or longer sulfurization anneal, narrows the bandgap of absorbers. (See Supplementary Fig. 1a–c for band gap (BG) tunability, as well as growth repeatability and homogeneity).

In what follows, absorbers with average 1.06 eV BG after buffer deposition were used (Fig. 2a). The process began under 750 mbar of nitrogen base pressure, had 1 °C/s heat up and cool down ramps, 10 min of RTP anneal at 520 °C and 1 min of sulfurization anneal under 50 mbar of pure H_2S, at 550 °C. The resulting narrow BG is consistent with the chemical composition of the absorbers, measured by EDX at 15 kV acceleration voltage—see Table 2. Indeed, following the BG calculation formula based on GGI and SSe ratios[27], the average composition estimates 1.05 eV of BG, which is roughly 10 meV different of the average extracted from PL response (1.06 eV). While these are reasonably in good agreement, any difference could be due to (i) lack of precision in BG estimation from EDX results, due to i.a., EDX detection limitations, and that it assumes an equal distribution of elements, while as will be seen, a compositional gradient is present, (ii) different probe depths in either of the techniques, (iii) the fact that EDX was done on bare absorbers, while PL was done on buffer-deposited absorber, which could result in a slightly larger value. This can be explained by removal of the native oxide, or passivation of defects, including oxygen vacancies or antistites[28]. Additionally, since either of the buffer layers contain sulfur, there could be some diffusion of S atoms from CdS or In_2S_3, into the absorber, hence widening the bandgap. Considering the 1 at% detection limit of the tool, the EDX indicates minimal incorporation of Ga in the first 1.25 μm of the absorber (probing depth calculated according to the Castaing formula[27,29], considering an average density of 5.07 g/cm^3, and using estimations presented by Baer et al.[30]). Such a hint of Ga segregation is in agreement with the known side-effect of the sequential growth, as seen in the literature, but also partly under the influence of the particular annealing regime employed (see BG tunability in Supplementary Fig. 1a). This is confirmed by the depth profile obtained for secondary ions under ToF-SIMS measurement (See Fig. 3a). Apart from the initial anomalies in response, which most likely stem from the (i) surface roughness, and (ii) changing the matrix of measurement at sample surface, the gallium profile gains more intensity towards the Mo back contact. This suggests the formation of a Ga back-graded CIGSSe. The small amount of added sulfur on the other hand, despite an overall steadier profile, still declines slightly towards the back of the absorber.

This segregation of the Ga at the back, and hence phase segregation, can also be inferred by comparing the XRD in locked couple (LC) and grazing incidence (GI) modes in Fig. 3b. The 112 peak shows a clear difference when comparing GI data, which extracts data from the surface, with LC data, which extracts data from and the bulk of the film. Firstly, the GI shows a slightly higher 2θ compared to LC, which could indicate either S or Ga presence at the surface[31]. However, given the front-rich sulfur profile, as opposed to the back-rich Ga profile, this shift can be probably attributed to S incorporation at the surface. Secondly, the surface sensitive measurement indicates the separation of 112 and 103 peaks while they start merging in the bulk measurement, suggesting an inclusion of Ga, in agreement with the ToF-SIMS. This interpretation goes hand in hand with the grain structures under cross section SEM observation—See Fig. 3d. Indeed, while grain sizes at the surface front approach CIGSSe film thickness, they tend to shrink towards the Mo interface. In other words, the Ga higher concentration at the back has resulted in smaller grains (more grains from more nucleation sites), and/or buildup of micro-strain inside the lattice, as also seen in other studies[32].

On the other hand, the rather large grains have contributed to the very high minority carrier lifetimes extracted by TRPL. Indeed, the measurements on both CdS and In_2S_3 samples showed lifetimes approaching 100 ns (Fig. 2b) in cases discussed here, and beyond 100 ns for samples with 1.00 eV bandgap (See Supplementary Fig. 1c, d). Besides the grains' contribution, the

Table 2 | Chemical composition of absorbers after selenization annealing

area	Ratios		Chemical composition (at%)				
	CGI	GGI	Cu	In	Ga	Se	S
1	0.93	0.06	23.9	24.3	1.4	47.9	2.5
2	0.89	0.03	22.2	24.3	0.8	50.0	2.8
3	0.95	0.04	22.1	22.4	1.0	52.3	3.2
Mean	0.92	0.04	22.7	23.7	1.1	50.1	2.8
Probe depth (μm)			1.25				

Measured with EDX at 15 kV acceleration voltage.

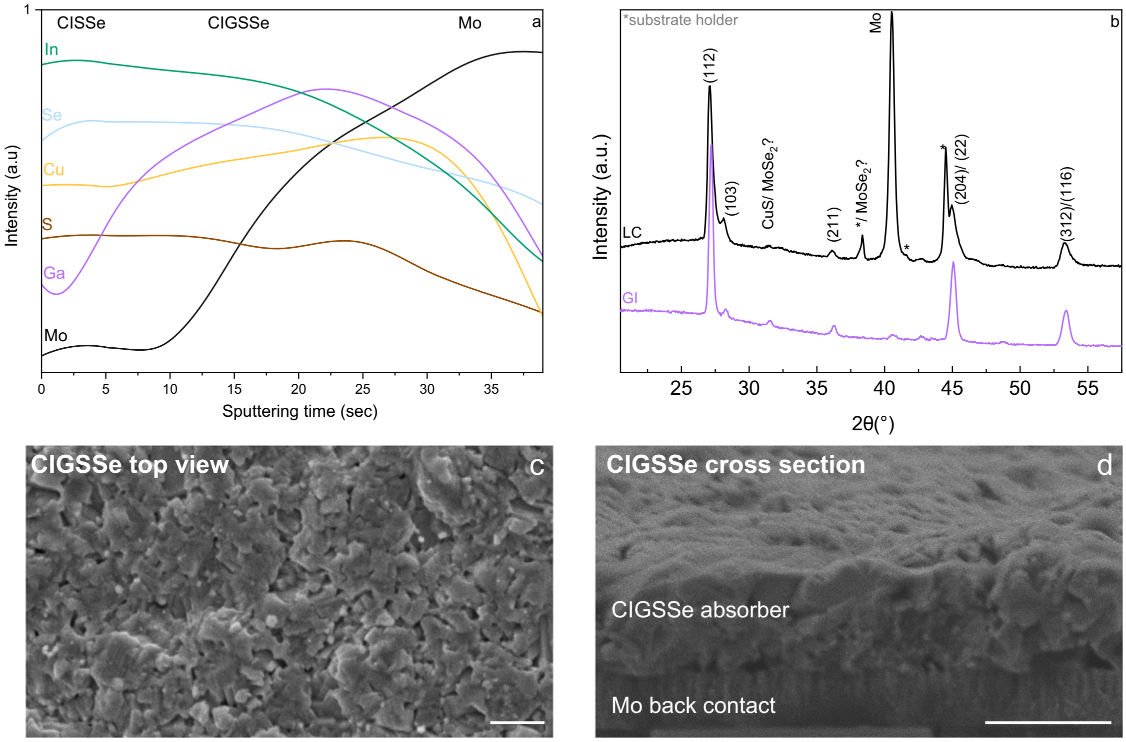

Fig. 3 | Composition, structure and morphology of as-grown CIGSSe absorbers. a Depth profile of absorber composition per ToF-SIMS measurement and (**b**) XRD and GI-XRD of the absorber layer on Mo. **c** Top view and (**d**) cross section SEM images. Scale bar in both cases is 2 µm.

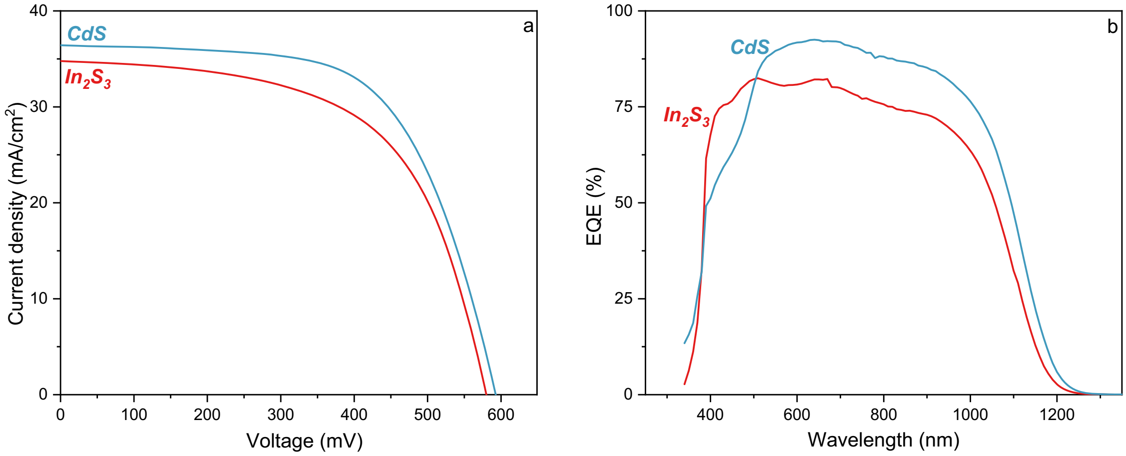

Fig. 4 | Photovoltaic performance solar cells with CdS and In_2S_3 buffer layers. a Current-Voltage behavior under AM1.5 G illumination and (**b**) and External Quantum Efficiency (EQE).

slight sulfurization proved essential in obtaining these long lifetime values (not shown). The In_2S_3 buffer showed slightly lower values, probably due to longer shelf time and exposure to air in the commute between labs. To the best of our knowledge, such high values of lifetime have not been reported for sequentially grown (flexible) CIGS solar cells and are comparable to other reported co-evaporated cousins[33–36].

The IV curves under AM1.5 G illumination for samples with CdS and In_2S_3 buffer are depicted in Fig. 4a, allowing to extract the efficiency (η in %), open-circuit voltage (V_{oc} in mV), short-circuit current density (J_{sc} in mA/cm^2) and fill factor (FF in %) shown in Fig. 4 along with the bandgap estimates from PL (E_g in eV) and values from similar studies. The shunt resistance (R_{sh} in $\Omega\,cm^2$), series resistance (R_s in $\Omega\,cm^2$), ideality factor (n), and saturation current density (J_0 in µA/cm^2) are obtained from the dark IV shown in Supplementary Fig. 2a. The EQE spectra for the CdS and In_2S_3 devices are shown in Fig. 4b, from which another estimation of J_{sc} is obtained and E_g is extrapolated using the derivative technique. The corresponding values are shown in Table 3 between brackets.

First, the similarity between the absorber bandgap values of 1.09 and 1.11 eV obtained via the EQE response of the CdS and In_2S_3 samples supports their comparability and the absorber process repeatability discussed previously. However, those estimates differ from the PL-extracted bandgap values by approximately 50 meV. For materials such as CIGS and kesterites, this is often the consequence of deep defects and crystalline disorder causing band tails[37]. In this case, characteristic Urbach energies close to 20 meV are observed for both samples (Supplementary Fig. 2b).

Another phenomenon might have as well caused this bandgap difference between EQE and PL, namely the segregation of Gallium towards the back surface, which could induce a slight bandgap gradient, which in turn would affect the estimation of the electrical bandgap from the EQE in comparison with the minimum optical bandgap from the PL. This could well be the case, given the Ga depth profile previously discussed. Second, one can observe a higher performance of the CdS-based device explained by higher V_{OC}, $J_{SC,}$ and FF, and lower R_s despite exhibiting poorer shunt, ideality factor, and saturation current density. The higher J_{SC} value reported for the CdS device from both light IV and EQE can be logically explained via the EQE spectra. Indeed, on the one hand, the parasitic absorption of the wider bandgap In_2S_3 buffer in the short wavelength region (350 to 500 nm) is lower than for CdS. On the other hand, the collection efficiency of photogenerated carriers beyond 500 nm seems degraded for the In_2S_3 device, eventually leading to overall lower J_{sc}, and potentially related to electronic losses at the absorber/buffer interface, as discussed in the next paragraph. This observation of lower EQE of the In_2S_3 solar cell, likely responsible for its lower FF than the CdS-based sample, appears to specifically hinder the collection of charges that are light-generated since the FF difference vanishes between dark IV curves shifted by J_{SC}, presented in Supplementary Fig. 2a. However, pushing this reasoning further to explain the poorer V_{OC} of the In_2S_3 device despite exhibiting better n and J_0 is not straightforward, solely based on IV measurements.

Indeed, different mechanisms could be responsible for restraining the collection of light-generated carriers after modifying the CdS buffer to In_2S_3, such as non-radiative recombination due to higher defect density or light-induced band misalignment creating a potential barrier. This is out of the scope of the present study but will hopefully motivate further investigations in the future. Still, the preliminary room temperature admittance measurements performed in this work could already enlighten the discussion.

Voltage-dependent admittance spectroscopy measurements are performed and represented as 2D "Capacitance-Voltage-frequency (CVf) loss maps"[38] in Fig. 5. The differences between the loss maps of CdS and In_2S_3 devices are quite striking. While the CdS cell's loss map is quite clean, meaning it shows no response of dominant loss mechanisms in the device's range of operation, the In_2S_3 sample exhibits a rather large response in the top right corner of its loss map. By comparing these experimental loss maps with simulated loss maps from[38], one could assimilate the broad response of the In_2S_3 device to an electronic defect or a potential barrier. Differentiating both would require further experiments and investigations, but the presence of such signature could contribute to explaining the poorer collection efficiency of In_2S_3 samples. Indeed, the red response that extends to frequencies beyond 10 kHz in Fig. 5b also happens to spread over the whole bias range between 0 V and V_{OC}, where its maximum lies.

Therefore, whichever the physical origin of the loss mechanism corresponding to the large response on the In_2S_3 device's loss map, it would likely affect the carrier collection in the voltage range where it is observed, i.e., the solar cell working regime. Given the unchanged structure and process of both types of devices except for the buffer layer, the FF degradation would probably relate to the absorber/buffer interface, e.g., an interface state or a band misalignment[38], rather than to the absorber bulk, which was shown to be homogeneous and reproducible above. Such an interface loss mechanism would likely contribute to V_{OC} degradation as well, through increased recombination, and could explain the observed V_{OC} discrepancy between both devices.

Overall, the performance of Cd-free low-bandgap CIGS solar cells based on inkjet printed In_2S_3 buffer is maintained to approximately 90% of the efficiency of standard CdS-based devices. The explanation for this slight reduction of PCE when changing the buffer from CdS to In_2S_3 resides in a slight reduction of all V_{OC}, $J_{SC,}$ and FF, for a reason seemingly related to photogenerated carrier collection but still requiring clarifications. Potential solutions to this issue are being investigated, such as interface passivation, heat treatment, and/or chemical etching to reconcile the performance of these flexible, non-toxic, low-bandgap CIS alternatives to standard solar cell designs. Overall, the results are quite promising, especially compared to the literature. Indeed, bendable devices reported here are on par with the best flexible single junction devices of any technology, with bandgaps below 1.1 eV[39]. Also, seeing Table 3, the efficiency of the CdS-based and In_2S_3-based

Table 3 | Absorber bandgap and solar cell parameters of record devices in this work versus similar studies

E_g (eV)	J_{sc} (mA/cm^2)	V_{oc} (mV)	FF (%)	η (%)	R_s (Ω.cm^2)	R_{sh} (Ω.cm^2)	n	J_0 (μA/cm^2)	Note
>1.13	31.2	544	66.1	11.2	~0.42	~4500	1.65	0.35	co-evap, iZO-AZO window[40]
—	35.0	455	52.0	8.3	—	—	—	—	two-step, iZO-ITO window[41]
—	27.0	630	61.3	10.5	2.65	513	—	—	co-evap, ITO back contact[42]
—	33.3	630	62.3	13.2	—	—	—	—	
1.05–1.1 (1.09)	36.4 (35.3)	593	62.3	13.5	1.34	1140	2.65	1.71	two-step, CdS$^{\text{this work record}}$
1.05–1.1 (1.11)	34.8 (31.5)	580	58.5	11.8	2.13	4381	2.22	0.51	two-step, $In_2S_3$$^{\text{this work record}}$

Missing information is noted with a slash (-). Estimates of J_{sc} and E_g obtained from the EQE spectra are shown between round brackets. For current-voltage measurements under dark conditions, see Supplementary Fig. 2.

Fig. 5 | Bias dependent, room temperature admittance spectroscopy of solar cells. 2D admittance spectroscopy "CVf loss map"[38,43], of the (**a**) CdS- and (**b**) In_2S_3-based samples.

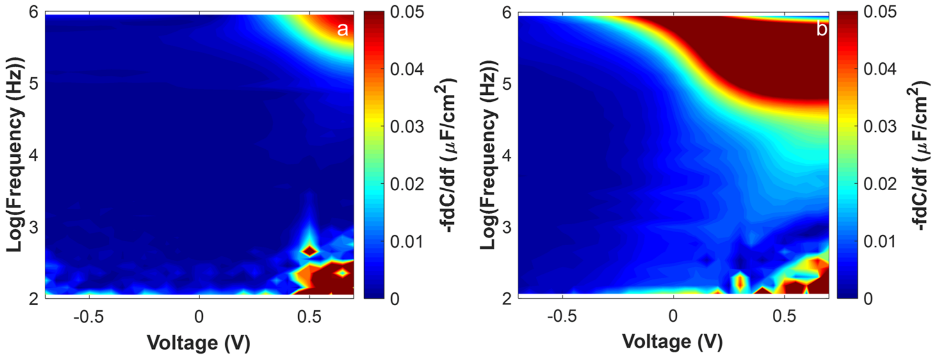

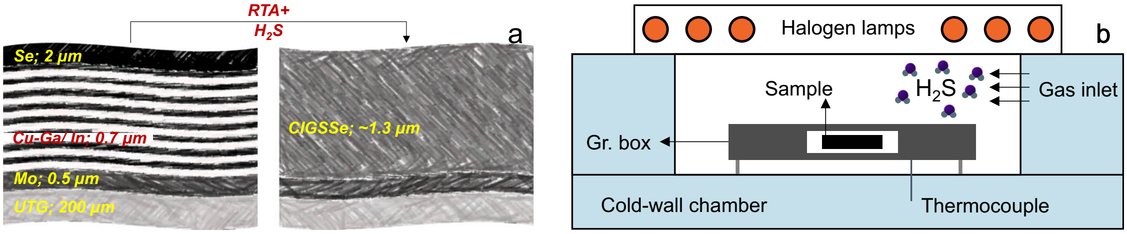

Fig. 6 | Methodology of absorber growth. Schematic of (**a**) absorber growth from a metallic precursor and (**b**) side view of the RTA furnace.

devices studied in this work surpasses the performance of similar CIGS devices[40,41] as well as bifacial solar cells[42]. While the lack of similar characterization hinders a comprehensive analogy, it is worth mentioning that, apart from one study[41], other references/studies have CIGSSe absorbers made via the co-evaporation route. The latter is usually considered to provide higher control over material quality than sequential processes such as the one presented herein. Though at module level, sequential growth still has the highest reported values[5].

Conclusion

Narrow bandgap CIGSSe has a high potential as bottom cell for double junction tandem technologies. Here, we demonstrate an adjusted sequential growth to synthesize gallium back-graded CIGSSe based devices on bendable UTG substrates. The simplicity and robustness of the process were discussed in terms of homogeneity within each sample, along with the repeatability of the method across multiple runs. The presented process is applicable to larger scales, short in duration (hence less cost intensive), and only limited by the furnace size in principle, and ramp rate control (since larger glass pieces typically need to be heated slower compared to small ones). Very promising absorbers were produced with a tunable bandgap between 1.00 and 1.11 eV, with high carrier lifetime, and moderate surface roughness. Moreover, high performing devices with the additional advantage of Cd-free buffer layers (In_2S_3) were also fabricated using a process with minimal waste (inkjet printing) compared to conventional CdS chemical bath deposition method.

With high scalability and process control, coupled with limited environmental impact from both material and process perspectives, such narrow bandgap CIGSSe absorbers have a great potential for emerging markets. For instance, emerging commercial spacecrafts or application integrated photovoltaics require flexible, lightweight, and high-power density solutions. Thin film tandem technology in particular can potentially address these requirements. In such a scheme, this work shows a way of enabling such products at an engineering level. There is of course room for improvement, primarily in further smoothening the absorber surface and optimizing its interface with the buffer layer. We believe a study on more conformal sputtering deposition, and more optimized precursor stack design (the metallic sandwich sequence and thickness), could show ways of improving the roughness of absorbers coming out of the RTA process.

Methods

200-micron thick borosilicate UTG, with a CTE of 7.4 ppm/K, was used as a substrate. It has an annealing point of 550 °C, refractive index of 1.523 (at 589.3 nm), and a density of 2.53 g/cm^3. 500 nm of sodium doped Mo was DC sputtered on the substrate, before a multilayer stack of Cu-Ga and In layers, with a total target thickness of 700 nm was RF sputtered. The CGI ([Cu]/([Ga]+[In])) and GGI ([Ga]/([Ga]+[In])) ratios after precursor deposition, measured by x-ray fluorescence technique, correspond to 0.83 and 0.30, respectively. This was followed by thermal evaporation of ~2 μm thick Se capping layer on top. The stack (Fig. 6a) was placed in a cold-wall rapid thermal annealing tool to grow the absorbers (Fig. 6b). The RTA has general attributes of high temperature annealing under a base pressure of N_2, and a short sulfurization via H_2S at the end to passivate the recombination centers. The whole growth step is done between 30 and 90 minutes, depending on the desired bandgap, and for devices reported here, under 45 minutes.

The as-grown absorber was cut into pieces (2.5 x 2.5 cm^2) for further processing. A p-n junction was subsequently formed by depositing either CdS (50 nm via chemical bath deposition) or In_2S_3 (synthesized similarly to the previous report[20], but with a modified solvents mixture (The thickness of the inkjet printed layer cannot be determined because of its porous morphology). As window layers, intrinsic ZnO and ITO were sputtered on the former, and ZnO and AZO on the latter, at 50 and 150 nm, and at 70 and 400 nm, respectively. A Ni/Ag/Ni sandwich of 50 nm was evaporated in the end to form front contacts, while 10 nm of Ni covered with 2 μm of Al was used for the In_2S_3 sample. Through mechanical scribing, cells were identified in 0.25 and 0.5 cm^2 effective areas for CdS and In_2S_3, respectively, and back contact was found by scratching the stack to Mo.

X-ray diffraction analysis (XRD), scanning electron microscopy (SEM) images, energy dispersive x-ray spectroscopy (EDX), steady-state and time-resolved Photoluminescence (TRPL), confocal optical microscopy (OM) imaging, and time of flight secondary ion mass spectroscopy (ToF-SIMS), were used for material characterization in terms of microstructure, morphology, composition, photoluminescence behavior, surface roughness, and composition depth profile, respectively. For device analysis, external quantum efficiency (EQE), current-voltage (I–V), and admittance spectroscopy were carried out. EQE was done in a custom-built tool, in dark and between 350 and 1300 nm, in 10 nm steps. The I–V measurement was done under AM 1.5 G spectra (Oriel solar simulator system class AAA) and via Keithley 2400 source meter and a 4-point probe setting, in air and at room temperature. For admittance spectroscopy, solar cells were measured at room temperature, under dark, from 1 kHz to 1 MHz, and with an AC voltage of 50 mV and a DC voltage bias range from −1 V to 1 V. The frequency range is covered logarithmically in 41 steps and the bias potential is linearly increased in steps of 50 mV.

XRD was done in locked couple (LC) and grazing incidence (GI) modes, with the latter done at 0.5°. In both cases, the 2θ ranged between 20 and 60°, and a step size of 0.5°. SEM imaging and EDX analysis were done using a TESCAN and Bruker system, at 10 kV and 15 kV acceleration voltage, respectively. For TRPL, a Picoquant FluoTime 300 system was employed, with an excitation wavelength of 532 nm, time resolution of 25 ps, and a repetition rate of 3 MHz. A laser-equipped Keyence confocal microscope was used for optical imaging and corresponding roughness measurements at 10 nm height steps. Time-of-flight secondary-ion mass spectrometry (ToF-SIMS) profiles were obtained with an TOFSIMS NCS from ION-TOF GmbH. Both positive and negative ion profiles were measured under Ar flooding (2e^{-6} bar), in a dual beam configuration via a Bi+ (15 keV) gun for analysis, on a 100 x 100 μm^2 raster area. Cs+ (2 keV) and O2+ (2 keV) sputtering guns were used for negative and positive ions, respectively.

Supporting Note

A supplementary file is available with more information on absorbers and solar cells.

Data availability

All data is available upon reasonable request.

Received: 27 February 2024; Accepted: 26 November 2024;
Published online: 06 January 2025

References

1. Robinson, K. S. *The Ministry for the Future*; Hachette UK, 2020.
2. Ruiz-Preciado, M. A. et al. Allegro, I. Monolithic Two-Terminal Perovskite/CIS Tandem Solar Cells with Efficiency Approaching 25%. *ACS Energy Lett.* **7**, 2273–2281 (2022).
3. Martulli, A. et al. Towards Market Commercialization: Lifecycle Economic and Environmental Evaluation of Scalable Perovskite Solar Cells. *Progress in Photovoltaics: Research and Applications n/a* (n/a). https://doi.org/10.1002/pip.3623.
4. Kim, S., Quy, H. V. & Bark, C. W. Photovoltaic Technologies for Flexible Solar Cells: Beyond Silicon. *Mater. Today Energy* **19**, 100583 (2021).
5. Green, M. A. et al. Solar Cell Efficiency Tables (Version 64). *Prog. Photovoltaics: Res. Appl.* **32**, 425–441 (2024).
6. Zhu, H. et al. Long-Term Operating Stability in Perovskite Photovoltaics. *Nat. Rev. Mater.* **8**, 569–586 (2023).
7. Afshari, H.; et al CIGS Solar Cells for Outer Planetary Space Applications: The Effect of Proton Irradiation. In *2020 47th IEEE Photovoltaic Specialists Conference (PVSC)*; 2020; pp 2635–2637. https://doi.org/10.1109/PVSC45281.2020.9300610.
8. Durant, B. K. et al. Tolerance of Perovskite Solar Cells to Targeted Proton Irradiation and Electronic Ionization Induced Healing. *ACS Energy Lett.* **6**, 2362–2368 (2021).
9. Krause, M. et al. Silver-Alloyed Low-Bandgap CuInSe2 Solar Cells for Tandem Applications. *Sol. RRL* **7**, 2201122 (2023).
10. Feurer, T. Narrow Band Gap Cu(In,Ga)Se2 for Tandem Solar Cell Application. Doctoral Thesis, ETH Zurich, https://doi.org/10.3929/ethz-b-000389221, 2019. .
11. Kessler, F. & Rudmann, D. Technological Aspects of Flexible CIGS Solar Cells and Modules. *Sol. Energy* **77**, 685–695 (2004).
12. Wuerz, R., Eicke, A., Kessler, F. & Pianezzi, F. Influence of Iron on the Performance of CIGS Thin-Film Solar Cells. *Sol. Energy Mater. Sol. Cells* **130**, 107–117 (2014).
13. Zortea, L. et al. Cu(In,Ga)Se2 Solar Cells on Low Cost Mild Steel Substrates. *Sol. Energy* **175**, 25–30 (2018).
14. Lopes, T. S. et al. Cu(In,Ga)Se2 Based Ultrathin Solar Cells the Pathway from Lab Rigid to Large Scale Flexible Technology. *npj Flex. Electron.* **7**, 4 (2023).
15. Hamtaei, S., Brammertz, G., Poortmans, J. & Vermang, B. A Review on Barrier Layers Used in Flexible Stainless-Steel Based CIGS Photovoltaic Devices. *npj Flex. Electron* **7**, 36 (2023).
16. Teloeken, A. C., Lamb, D. A., Dunlop, T. O. & Irvine, S. J. C. Effect of Bending Test on the Performance of CdTe Solar Cells on Flexible Ultra-Thin Glass Produced by MOCVD. *Sol. Energy Mater. Sol. Cells* **211**, 110552 (2020).
17. Dou, B. et al. High-Performance Flexible Perovskite Solar Cells on Ultrathin Glass: Implications of the TCO. *J. Phys. Chem. Lett.* **8**, 4960–4966 (2017).
18. Brew, K. W., McLeod, S. M., Garner, S. M. & Agrawal, R. Improving Efficiencies of Cu2ZnSnS4 Nanoparticle Based Solar Cells on Flexible Glass Substrates. *Thin Solid Films* **642**, 110–116 (2017).
19. Garner, S. M. *Flexible Glass: Enabling Thin, Lightweight, and Flexible Electronics*; John Wiley & Sons, 2017.
20. Debot, A. et al. Inkjet-Printed Indium Sulfide Buffer Layer for Cu(In,Ga)(S,Se)2 Thin Film Solar Cells. *Thin Solid Films* **745**, 139096 (2022).
21. Chu, V. B. et al. Waste- and Cd-Free Inkjet-Printed Zn(O,S) Buffer for Cu(In,Ga)(S,Se)$_2$ Thin-Film Solar Cells. *ACS Appl. Mater. Interfaces* **13**, 13009–13021 (2021).
22. Elanzeery, H. et al. Beyond 20% World Record Efficiency for Thin-Film Solar Modules. *IEEE J. Photovolt.* **14**, 107–115 (2024).
23. Hultqvist, A. et al. Performance of Cu(In,Ga)Se2 Solar Cells Using Nominally Alkali Free Glass Substrates with Varying Coefficient of Thermal Expansion. *J. Appl. Phys.* **114**, 094501 (2013).
24. Gerthoffer, A. et al. CIGS Solar Cells on Ultra-Thin Glass Substrates: Determination of Mechanical Properties by Nanoindentation and Application to Bending-Induced Strain Calculation. *Sol. Energy Mater. Sol. Cells* **166**, 254–261 (2017).
25. Kafedjiska, I. et al. Integration of Rough RTP Absorbers into CIGS-Perovskite Monolithic Tandems by NiOx(:Cu)+SAM Hole-Transporting Bi-Layers. *Sol. Energy Mater. Sol. Cells* **254**, 112248 (2023).
26. Han, Q. et al. High-Performance Perovskite/Cu(In,Ga)Se$_2$ Monolithic Tandem Solar Cells. *Science* **361**, 904–908 (2018).
27. Bär, M. et al. Determination of the Band Gap Depth Profile of the Penternary Cu(In(1 − X)GaX)(SYSe(1 − Y))2 Chalcopyrite from Its Composition Gradient. *J. Appl. Phys.* **96**, 3857–3860 (2004).
28. Shirakata, S., Ohkubo, K., Ishii, Y. & Nakada, T. Effects of CdS Buffer Layers on Photoluminescence Properties of Cu(In,Ga)Se2 Solar Cells. *Sol. Energy Mater. Sol. Cells* **93**, 988–992 (2009).
29. Castaing, R. Application Des Sondes Électroniques à Une Méthode d'analyse Ponctuelle Chimique et Cristallographique. *These Universite de Paris 1951* **1952**.
30. Baer, M. et al. Determination of the band gap depth profile of the penternary Cu(In(1-X)GaX)(SYSe(1-Y))2 chalcopyrite from its composition gradient. *J. Appl. Phys.* **96**, 3857–3860 (2004).
31. Malaquias, J. C. et al. Controlled Bandgap CuIn 1−x Ga x (S 0.1 Se 0.9) 2 (0.10 ≤ x ≤ 0.72) Solar Cells from Electrodeposited Precursors. *Thin Solid Films* **582**, 2–6 (2015).
32. Abou-Ras, D. et al. Impact of the Ga concentration on the microstructure of CuIn1–x Gax Se2. *Phys. status solidi (RRL)–Rapid Res. Lett.* **2**, 135–137 (2008).
33. Kamikawa, Y., Nishinaga, J., Shibata, H. & Ishizuka, S. Efficient narrow band gap Cu(In,Ga)Se2 solar cells with flat surface. *ACS Appl. Mater. Interfaces* **12**, 45485–45492 (2020).
34. Wands, J. et al. Evaluating Recombination Mechanisms in RbF Treated Cu(InxGa1-x)Se2 Solar Cells. *IEEE J. Photovoltaics* 12, 1400–1405 (2022). .
35. Yang, S.-C. et al. Influence of Ga back grading on voltage loss in low-temperature co-evaporated Cu(In,Ga)Se2 thin film solar cells. *Prog. Photovoltaics: Res. Appl.* **29**, 630–637 (2021).
36. Ochoa, M., Yang, S.-C., Nishiwaki, S., Tiwari, A. N. & Carron, R. Charge carrier lifetime fluctuations and performance evaluation of Cu(In,Ga)Se2 absorbers via time-resolved-photoluminescence microscopy. *Adv. Energy Mater.* **12**, 2102800 (2022).
37. Siebentritt, S. et al. What Is the Bandgap of Kesterite? *Sol. Energy Mater. Sol. Cells* **158**, 126–129 (2016).
38. Brammertz, G. et al. Bias-dependent admittance spectroscopy of thin-film solar cells: experiment and simulation. *IEEE J. Photovolt.* **10**, 1102–1111 (2020).
39. Almora, O. et al. Device Performance of Emerging Photovoltaic Materials (Version 3. Advanced Energy Materials 13, 2203313 (2023).
40. Gerthoffer, A. et al. CIGS solar cells on flexible ultra-thin glass substrates: characterization and bending test. *Thin Solid Films* **592**, 99–104 (2015).
41. Chen, J. et al. Performance and stability enhancement of Cu(InGa)Se2 solar cells on ultrathin glass by potassium incorporation. *Mater. Lett.* **271**, 127749 (2020).
42. Kim, D. et al. Flexible and semi-transparent ultra-thin CIGSe solar cells prepared on ultra-thin glass substrate: a key to flexible bifacial photovoltaic applications. *Adv. Funct. Mater.* **30**, 2001775 (2020).
43. Kohl, T. et al. Bias dependent admittance spectroscopy of thin film solar cells: KF post deposition treatment, accelerated lifetime testing, and their effect on the CVf loss maps. *Sol. Energy Mater. Sol. Cells* **231**, 111289 (2021).

Acknowledgements

This work received funding from the European Union's Horizon 2020 research and innovation program under grant agreement No. 850937. S.H. and R.S. acknowledge financial support by the Flanders Research Foundation (FWO)—strategic basic research doctoral grant 1S31922N, and fundamental research doctoral grant 1178022 N, respectively. A.D. acknowledges financial support from the Fond National de la Recherche of Luxembourg through the STARSOL (C18/MS/12686759) grant. The authors also thank Tim Oris, Maarten van der Vleuten, Alexis Franquet and Rita Tilmann for their help with processing, measurements, and other valuable discussions.

Author contributions

S.H. and G.B. conceptualized the work. S.H., A.D., R.S., and E.C., conducted the experiments, measurements, and data analysis. S.H., R.S., and A.D. wrote the original manuscript. G.B., P.D., A.A., S.G., J.P., and B.V. reviewed and edited the original draft. B.V., P.D., and S.G. provided resources and project administration. The authors declare no competing interests.

Competing interests

The authors declare no competing interests.

Additional information

Supplementary information The online version contains supplementary material available at https://doi.org/10.1038/s43246-024-00706-x.

Correspondence and requests for materials should be addressed to Sarallah Hamtaei.

Peer review information *Communications materials* thanks the anonymous reviewers for their contribution to the peer review of this work.

Reprints and permissions information is available at http://www.nature.com/reprints